

# A 2.4 GHz 4 mW Integer-N Inductorless RF Synthesizer

Long Kong, *Student Member, IEEE*, and Behzad Razavi, *Fellow, IEEE*

**Abstract**—The high phase noise of ring oscillators has generally discouraged their use in RF synthesis. This paper introduces an integer-N synthesizer that employs a type-I loop to achieve a wide bandwidth, allowing the use of ring oscillators, and a master-slave sampling loop filter along with harmonic traps to suppress spurs. A 2.4 GHz prototype fabricated in 45 nm digital CMOS technology provides a loop bandwidth of 10 MHz and a spur level of  $-65$  dBc. The phase noise is  $-114$  dBc/Hz at 1 MHz offset.

**Index Terms**—Frequency synthesizer, harmonic trap, phase-locked loop (PLL), reference spur, voltage-controlled oscillator (VCO),  $\Delta$  modulator.

## I. INTRODUCTION

RF SYNTHESIS has generally shied away from ring oscillators due to their much more severe phase noise-power trade-offs than those of LC topologies. Today's multiband, multimode radios, however, require a number of synthesizers and can greatly benefit from compact, flexible implementations afforded by ring oscillators.

This paper proposes a phase-locked loop (PLL) architecture that can achieve a wide loop bandwidth, thus suppressing the voltage-controlled oscillator (VCO) phase noise and allowing the use of a ring topology. An integer-N synthesizer based on this architecture also incorporates “harmonic traps” on the VCO control line to reduce the output sidebands [1]. Most of the concepts introduced here are applicable to other PLL and oscillator topologies as well. Implemented in the TSMC 45 nm digital CMOS technology, an experimental prototype exhibits a phase noise of  $-114$  dBc/Hz up to 10 MHz offset with a spur level of  $-65$  dBc.

Section II provides the motivation for this work and reviews the bandwidth limitations of traditional PLLs. Section III describes the evolution of the proposed synthesizer architecture. Section IV deals with phase noise considerations, and Section V is concerned with spur reduction. Section VI presents the experimental results.

Manuscript received August 24, 2015; revised December 14, 2015; accepted December 17, 2015. Date of publication February 05, 2016; date of current version March 02, 2016. This paper was approved by Associate Editor Waleed Khalil. This work was supported in part by the Qualcomm Innovation Fellowship Program, in part by the Broadcom Fellowship Program, and in part by Realtek Semiconductor.

The authors are with the Department of Electrical Engineering, University of California, Los Angeles, CA 90095-1594 USA (e-mail: razavi@ee.ucla.edu).

Color versions of one or more of the figures in this paper are available online at <http://ieeexplore.ieee.org>.

Digital Object Identifier 10.1109/JSSC.2015.2511157

## II. BACKGROUND

### A. General Considerations

The need for LC oscillators in RF synthesis has been solidified by various studies revealing that the white-noise-induced phase noise of ring oscillators trades primarily with the power consumption [2], [3] and is relatively independent of the number of stages. However, ring oscillators do present compelling advantages. 1) They occupy a smaller area and can be readily placed within a transceiver layout with less serious concerns regarding proximity effects. 2) They entail much less coupling to and from other circuits. 3) They achieve a wider tuning range and can be multiplexed to cover decades of frequencies. 4) They readily generate multiple phases.

That the phase noise of ring oscillators is difficult to improve at the circuit level forces us to higher levels of abstraction. For example, [4] processes the signals in an RF receiver (RX) so as to suppress the phase noise in reciprocal mixing. This approach, however, does not correct for the effect of phase noise on the received signal constellation and the error vector magnitude (EVM) (e.g., in the absence of a blocker), nor is it applicable to the transmitter (TX). It is interesting to note that 1) applications entailing significant reciprocal mixing, e.g., GSM, actually place tighter requirements on the TX phase noise, and 2) applications specifying the phase noise by the EVM, e.g., IEEE 802.11 a/b/g, impose equally stringent phase noise constraints on RX and TX. In other words, the TX phase noise is at least as critical as the RX phase noise in most systems. It is therefore desirable to seek a solution that can be applied to both.

### B. PLL Bandwidth Limitations

Another level of abstraction at which phase noise reduction can be considered is the synthesizer architecture. The loop bandwidth is generally constrained by three factors: 1) the PLL reference frequency,  $f_{\text{REF}}$ ; for example, in a mobile phone environment, only a crystal oscillator around 20 MHz is available; 2) the PLL stability limit, often called “Gardner’s Limit,” and generally accepted to be around  $f_{\text{REF}}/10$  for type-II topologies; and 3) the ripple amplitude on the VCO control line and hence the output spur level. In the presence of charge pump (CP) non-idealities, the loop bandwidth is reduced to typically  $f_{\text{REF}}/20$  or less if spurs lower than  $-60$  dBc are required [5]–[9].

It is helpful to briefly review the different bandwidths encountered in PLL analysis: 1) the input–output transfer function has a certain 3 dB bandwidth, which we call the “PLL bandwidth”  $f_{\text{BW}}$  in this paper; 2) the loop transmission has

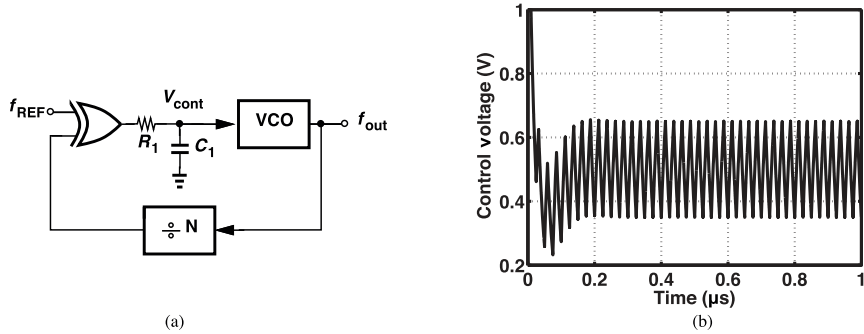


Fig. 1. (a) Traditional type-I PLL architecture. (b) Settling behavior with bandwidth of 5.6 MHz.

a unity-gain bandwidth  $f_{\text{UGB}}$ ; and 3) the VCO noise transfer function, a high-pass response, also has a 3 dB bandwidth  $f_{n, \text{VCO}}$ . For example, a type-II PLL with a charge pump current  $I_p$ , a loop filter capacitor  $C_1$ , a VCO gain  $K_{\text{VCO}}$ , a divide ratio  $N$ , and a unity damping factor provides  $2\pi f_{\text{BW}} \approx 2.5\omega_n = 2.5\sqrt{I_p K_{\text{VCO}} / (2\pi N C_1)}$ ,  $2\pi f_{\text{UGB}} \approx 2.1\omega_n$ , and

$$2\pi f_{n, \text{VCO}} \approx 1.55\omega_n. \quad (1)$$

For example, if  $f_{\text{UGB}}$  is chosen in the range of  $f_{\text{REF}}/20$  to  $f_{\text{REF}}/10$ , then

$$0.037f_{\text{REF}} < f_{n, \text{VCO}} < 0.074f_{\text{REF}}. \quad (2)$$

As mentioned above, [5]–[9] choose a loop bandwidth less than  $f_{\text{REF}}/20$ , thus falling on the low side of (2).

### III. PROPOSED WIDEBAND PLL

Our approach to suppressing the VCO phase noise is to develop a PLL topology that avoids Gardner’s limit and, if necessary, deal with the ripple on the control voltage by additional techniques. We assume  $f_{\text{REF}} = 20$  MHz. Let us consider a type-I PLL architecture. Shown in Fig. 1(a), such a loop contains only one integrator and can, in principle, remain stable with a wide bandwidth. For example, Fig. 1(b) depicts the circuit’s transient behavior with  $(R_1 C_1)^{-1} = 2\pi(40 \text{ MHz})$ ,  $K_{\text{VCO}} = 1500 \text{ MHz/V}$ ,  $N = 120$ , and hence a loop bandwidth of 5.6 MHz. Of course, since the exclusive-OR (XOR) output swings from 0 to  $V_{\text{DD}}$ , the VCO experiences a large ripple. In fact, as  $R_1 C_1$  is reduced, the theoretical loop bandwidth can even exceed  $f_{\text{REF}}/2$ , but, as plotted in Fig. 2, the spurs eventually rise *above* the carrier, rendering the circuit meaningless. This PLL sustains a static phase error in proportion to the oscillator control voltage. For a  $V_{\text{cont}}$  ranging from 0 to  $V_{\text{DD}}$ , this error varies from 0 to about  $180^\circ$ .

The type-I PLL also suffers from a limited capture range. If the VCO begins with a frequency of  $f_1$  and the XOR output at  $|f_1/N - f_{\text{REF}}|$  is heavily attenuated by the filter, then the loop has no tendency to lock. In the foregoing example,  $(R_1 C_1)^{-1}$  must be lowered to  $2\pi(0.47 \text{ MHz})$  for the output spurs to fall to  $-35.5 \text{ dBc}$ , yielding a simulated capture range of about 7.4%.

#### A. Type-I PLL with Sampling Filter

In a manner similar to charge-pump PLLs [10], [11], we can replace the continuous-time filter in Fig. 1(a) with a

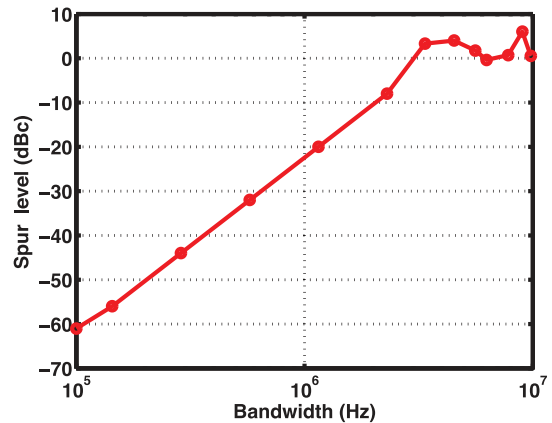


Fig. 2. Spur level versus bandwidth for type-I PLL.

discrete-time implementation, aiming to isolate the VCO from the large XOR jumps. As depicted in Fig. 3(a), we wish to select the timing between the main input and  $V_F$  such that  $S_0$  turns ON only during a “settled” level. Unfortunately, this is not possible because  $V_X$  still jumps between 0 and  $V_{\text{DD}}$ . Fig. 3(b) shows the loop’s waveforms in the locked condition, indicating that  $V_X$  varies at  $2f_{\text{REF}}$  if the input has a 50% duty cycle. When  $V_F$  goes high,  $V_{\text{cont}}$  attempts to track  $V_X$ , reaching a certain level  $V_1$  that is necessary for the VCO to operate at  $Nf_{\text{REF}}$ .<sup>1</sup> That is, the loop adjusts the phase error  $\Delta\phi$ , until the  $V_{\text{cont}}$  transient yields a value of  $V_1$  at the end of one  $T_{\text{REF}}$ .

The above technique does provide a constant voltage  $V_1$ , for the VCO while  $S_0$  is off. We therefore wish to modify the circuit so that the VCO does not sense the transient from  $t_1$  to  $t_2$ . This is accomplished by inserting one more sampling network in the VCO control path [Fig. 4(a)], with the two now operating in a master–slave manner. The divider output is converted to two nonoverlapping phases, preventing direct feedthrough from  $V_X$  to  $V_{\text{cont}}$ . We expect to observe a large ripple on  $C_1$ , similar to that in Fig. 3(b), but a small ripple on  $C_2$ . As an example, Fig. 4(b) shows the transient behavior with  $C_1 = 16 \text{ pF}$ ,  $C_2 = 1 \text{ pF}$ ,  $K_{\text{VCO}} = 280 \text{ MHz/V}$ , and  $N = 120$ . The loop bandwidth is about 9 MHz and the loop settles in roughly 10 input cycles.

The PLL architecture employing the master–slave sampling filter (MSSF) displays several interesting and useful properties.

<sup>1</sup>This is true only if the ripple is small.

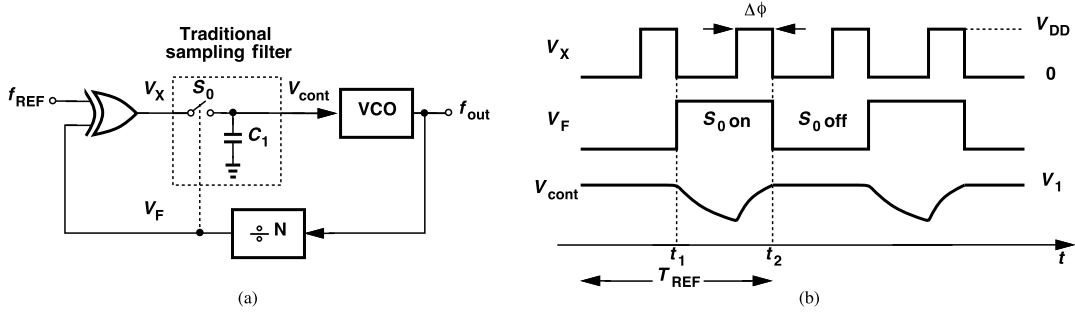


Fig. 3. (a) Type-I PLL with traditional sampling filter. (b) Time-domain operation.

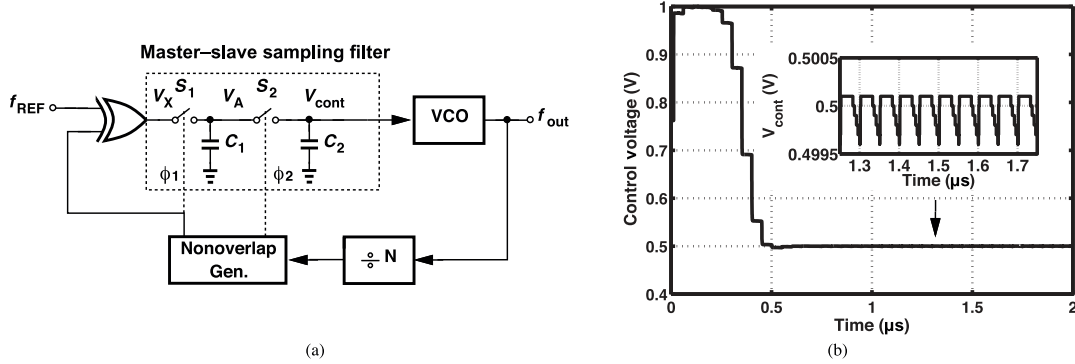


Fig. 4. Proposed PLL (a) architecture, and (b) settling behavior.

As explained below, compared to the traditional type-I PLL, its capture range is much wider, and, in comparison to type-II PLLs, it achieves a loop bandwidth close to  $f_{\text{REF}}/2$ , settles faster, and avoids the difficulties in low-voltage CP design.

### B. MSSF Transfer Function

As explained above, the periodic voltage jumps at  $V_X$  in Fig. 4(a) do not reach  $V_{\text{cont}}$ , implying that the master-slave filter response has notches at the reference frequency and its harmonics. We examine this response in detail here.

As a continuous-time (CT) approximation, we can say that  $C_1$  switches between  $V_X$  and  $V_{\text{cont}}$  periodically, thus acting as a series resistor  $R_{\text{eq}}$  equal to  $1/(f_{\text{CK}}C_1)$ , where  $f_{\text{CK}}$  denotes the sampling frequency and is equal to  $f_{\text{REF}}$  when the loop reaches the locked condition. In other words, the filter resembles a first-order section having a response given by

$$H(s) = \frac{1}{1 + R_{\text{eq}}C_2s} = \frac{1}{1 + \frac{C_2}{C_1f_{\text{CK}}}s}. \quad (3)$$

Note that this response accounts for charge sharing between  $C_1$  and  $C_2$ , but fails to predict the harmonic notches. It is also a crude approximation if the PLL bandwidth approaches  $f_{\text{REF}}/2$ .

A more accurate transfer function is obtained if we consider the MSSF as a zero-order hold (ZOH) circuit. As illustrated in Fig. 5, the circuit converts a CT input to a discrete-time output. If  $C_2 \ll C_1$  so that charge sharing between the two capacitors can be neglected, then the ZOH output can be expressed as [12]

$$Y(f) = e^{-j2\pi fT_{\text{CK}}/2} \frac{\sin \pi fT_{\text{CK}}}{\pi fT_{\text{CK}}} \sum_{n=-\infty}^{\infty} X\left(f - \frac{n}{T_{\text{CK}}}\right). \quad (4)$$

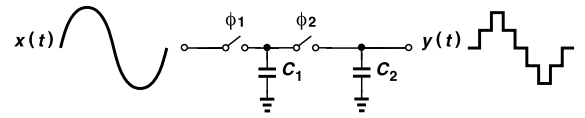


Fig. 5. Input and output waveforms of MSSF with zero switch resistance.

For the output component of interest,  $n = 0$  and

$$Y_0(f) = e^{-j2\pi fT_{\text{CK}}/2} \frac{\sin \pi fT_{\text{CK}}}{\pi fT_{\text{CK}}} X(f). \quad (5)$$

This result, of course, predicts the notches at the harmonic of  $f_{\text{CK}}$  but disregards charge sharing.<sup>2</sup>

Even though operating as a master-slave storage circuit, the proposed filter exhibits a delay of  $T_{\text{CK}}/2$ , rather than  $T_{\text{CK}}$ , in the PLL environment. This is because the XOR produces the phase error information twice per cycle. Illustrated in Fig. 6, this effect can be seen by displacing the  $f_{\text{REF}}$  edges by a small amount  $\Delta T$  and observing that  $V_X$  inherits this change from both the rising edge and the falling edge of  $V_{\text{in}}$ . Consequently,  $V_A$  changes in about  $T_{\text{CK}}/2$  seconds and is frozen thereafter. If the MSSF delay were as long as  $T_{\text{CK}}$ , the PLL would become unstable for a unity-gain bandwidth of  $f_{\text{REF}}/4$ .

Equation (5) is a reasonable MSSF model for our analysis and design efforts described below, especially because we will select  $C_2$  much less than  $C_1$ , thus minimizing charge sharing and improving the ZOH approximation. However, a more

<sup>2</sup>A  $z$ -domain model can also be constructed but yielding less intuition in terms of stability and closed-loop behavior (Sections III-C and III-D).

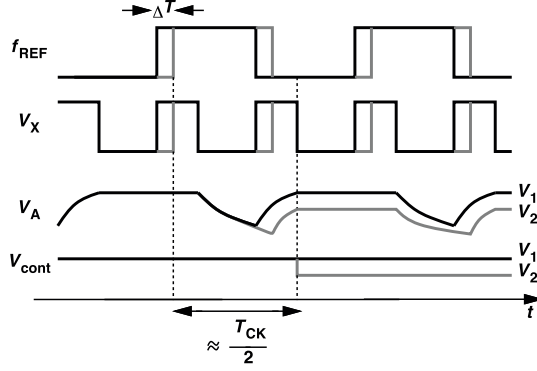


Fig. 6. XOR and MSSF time-domain waveforms.

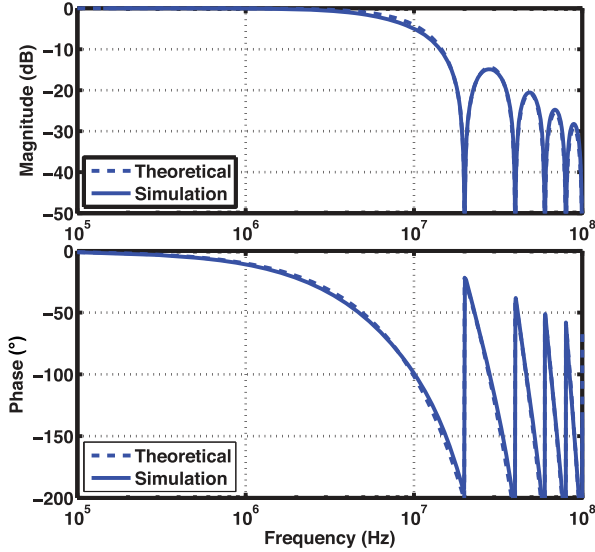


Fig. 7. Magnitude and phase responses of MSSF.

accurate model, obtained empirically, is as follows:

$$H_{\text{MSSF}}(j\omega) = \frac{1}{1 + \frac{C_2}{C_1 f_{\text{CK}}} j\omega} e^{-j\pi f T_{\text{CK}}} \frac{\sin \pi f T_{\text{CK}}}{\pi f T_{\text{CK}}}. \quad (6)$$

Plotted in Fig. 7 are the magnitude and phase of the MSSF transfer function as predicted by (6) and as obtained from transient circuit simulations. Here,  $C_1 = 16$  pF,  $C_2 = 1$  pF, and  $f_{\text{REF}} = 20$  MHz. We observe good agreement between the two. In this example, the filter has a 3 dB bandwidth of 7.4 MHz, at which the phase shift reaches  $-75^\circ$ . To minimize this phase shift (which affects the loop stability), we typically choose  $C_1 \gg C_2$  and reduce the contribution of the first fraction in (6).

The deep notches in Fig. 7 distinguish the MSSF from continuous-time filters. These notches suppress the harmonic components generated by the XOR gate in Fig. 4(a), thereby easing the trade-off between the loop bandwidth and the ripple amplitude. Nonetheless, second-order effects do create some ripple and are addressed in Section V.

### C. Stability Considerations

While greatly suppressing the ripple, our proposed PLL is not unconditionally stable. In this section, we deal with this point.

From (6), the loop transmission of the topology shown in Fig. 4(a) can be expressed as

$$H(j\omega) = \frac{K_{\text{PD}} K_{\text{VCO}}}{N} \times \frac{1}{j\omega} \times \frac{1}{1 + \frac{C_2}{C_1 f_{\text{REF}}} j\omega} e^{-j\pi f T_{\text{REF}}} \frac{\sin \pi f T_{\text{REF}}}{\pi f T_{\text{REF}}} \quad (7)$$

where  $K_{\text{PD}}$  is the phase detector (PD) gain (chosen approximately equal to 2.2 V/rad so as to provide the desired bandwidth). We have approximated the MSSF sampling rate by  $f_{\text{REF}}$ . To determine the phase margin, we must examine  $\angle H(j\omega)$  at the unity-gain bandwidth  $f_{\text{UGB}}$ , i.e., the frequency at which  $|H(j\omega)|$  drops to unity. To this end, we make two approximations. 1) As explained in Section III-B,  $C_1 \gg C_2$  and hence the fraction  $1/[1 + C_2 j\omega/(C_1 f_{\text{REF}})]$  contributes negligibly to  $\angle H$  and  $|H|$ . 2) Predicting that  $f_{\text{UGB}} < f_{\text{REF}}/2$ , we also neglect the effect of the sinc on  $|H|$ . It follows that  $|H(j\omega)| \approx K_{\text{PD}} K_{\text{VCO}}/(N\omega)$  and  $2\pi f_{\text{UGB}} \approx K_{\text{PD}} K_{\text{VCO}}/N$ . The phase contains a  $-90^\circ$  contribution by the VCO and  $-\pi f T_{\text{REF}}$  by the MSSF,  $\angle H(j\omega) \approx -\pi/2 - \pi f T_{\text{REF}}$ . The phase margin  $\pi + \angle H(j2\pi f_{\text{UGB}})$  is thus equal to

$$\text{PM} = \frac{\pi}{2} - \pi f_{\text{UGB}} T_{\text{REF}} = \frac{\pi}{2} - \frac{K_{\text{PD}} K_{\text{VCO}}}{2N} T_{\text{REF}}. \quad (8)$$

Equation (8) imposes an upper bound of  $f_{\text{REF}}/2$  on  $f_{\text{UGB}}$ . The phase margin reaches about  $45^\circ$  for  $f_{\text{UGB}} = f_{\text{REF}}/4$ .

### D. Closed-Loop Behavior

As mentioned in Section II, the closed-loop input-output bandwidth and the VCO noise transfer bandwidth are of interest. For the former, we have

$$\frac{\phi_{\text{out}}}{\phi_{\text{in}}}(j\omega) = \frac{NH(j\omega)}{1 + H(j\omega)}. \quad (9)$$

With the approximation stipulated in Section III-C,  $H(j\omega) \approx [K_{\text{PD}} K_{\text{VCO}}/(Nj\omega)] \exp(-j\pi f T_{\text{REF}})$ . As shown in Appendix I, the 3 dB bandwidth is obtained as

$$2\pi f_{\text{BW}} \approx 2\sqrt{3} f_{\text{REF}} \sqrt{\frac{\alpha - 1 + \sqrt{(\alpha - 1)^2 + \alpha^3/6}}{\alpha}} \quad (10)$$

where  $\alpha = 2\pi f_{\text{UGB}}/f_{\text{REF}}$ . Recall from (8) that  $f_{\text{REF}}/4 < f_{\text{UGB}} < f_{\text{REF}}/2$  for  $45^\circ > \text{PM} > 0$ , i.e.,  $\pi/2 < \alpha < \pi$ . For this range of  $\alpha$ , we have

$$0.55 f_{\text{REF}} < f_{\text{BW}} < 0.71 f_{\text{REF}}. \quad (11)$$

The key point here is that the closed-loop bandwidth can reach  $f_{\text{REF}}/2$  with a reasonable phase margin.

The wide bandwidth of the proposed PLL naturally translates to a fast lock transient, e.g., about 10 input cycles as shown in Fig. 4(b).

For the VCO noise transfer, we have  $\phi_{\text{out}}/\phi_{\text{VCO}} = (1 + H)^{-1}$ . The 3 dB bandwidth is obtained as

$$2\pi f_{n, \text{VCO}} \approx 2\sqrt{3} f_{\text{REF}} \sqrt{\frac{\alpha + 1 - \sqrt{(\alpha + 1)^2 - \alpha^3/6}}{\alpha}} \quad (12)$$

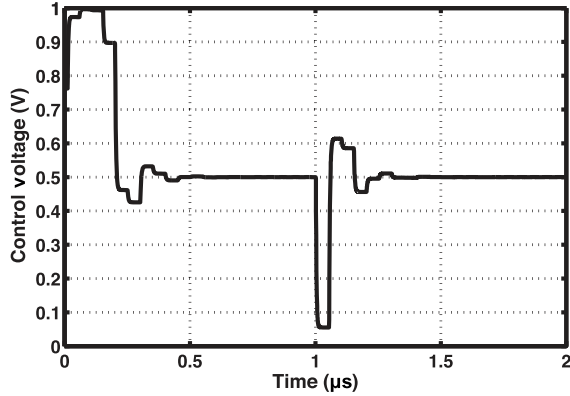


Fig. 8. Simulated control voltage with an input phase step at 1  $\mu$ s.

which, for  $\pi/2 < \alpha < \pi$ , falls in the range of

$$0.16f_{\text{REF}} < f_{n, \text{VCO}} < 0.26f_{\text{REF}}. \quad (13)$$

For a fair comparison, we consider only the lower bound and note that, with respect to the two limits prescribed by (2), we have improved the VCO noise suppression bandwidth by about a factor of 2.2 to 4.3. In our synthesizer design,  $f_{n, \text{VCO}} \approx 0.17f_{\text{REF}}$  for a PM of around  $42^\circ$ . Fig. 8 shows the simulated settling behavior when PLL input experiences a phase step at 1  $\mu$ s.

#### E. Acquisition Range

The MSSF-based PLL provides a much wider acquisition range than the traditional type-I architecture. Fundamentally, this is because the MSSF in Fig. 4(a) is clocked by the feedback signal, thus behaving differently from the continuous-time filter during the acquisition process. In order to formulate the acquisition range, we construct the open-loop configuration shown in Fig. 9(a), assuming that the VCO operates at a frequency of  $f_1$ . We follow the “beat” component generated by the XOR gate,  $f_1/N - f_{\text{REF}}$ , through the sampling filter and consider two cases. First, suppose the sampling process satisfies the Nyquist rate, i.e.,  $|f_1/N - f_{\text{REF}}| < f_1/(2N)$  and hence  $(2/3)f_{\text{REF}} < f_1/N < 2f_{\text{REF}}$ . In this case, the beat component passes through as a “baseband” signal, providing a nearly rail-to-rail voltage swing to the VCO. Fig. 9(b) plots the simulated control voltage in such a scenario; the VCO is heavily modulated at a rate of  $f_1/N - f_{\text{REF}}$ , producing a strong sideband at the divider output located at  $f_1/N - (f_1/N - f_{\text{REF}}) = f_{\text{REF}}$ .<sup>3</sup> In the closed-loop configuration, this sideband yields a dc component at the XOR output, leading to acquisition. The above inequality can be referred to the output as  $(2/3)Nf_{\text{REF}} < f_1 < 2Nf_{\text{REF}}$ . The loop therefore locks for an initial frequency between 2/3 and 2 times the final value. For example, if the VCO tuning range is from 1.6 to 4.8 GHz, then the loop can always lock to 2.4 GHz. The second case arises if the beat experiences aliasing, i.e., if  $f_1/N$  falls outside the acquisition range. The MSSF output now contains a component at  $f_1/N - |f_1/N - f_{\text{REF}}|$ , which does

<sup>3</sup>MSSF sampling clock too carries sidebands, but they negligibly contribute to the MSSF output.

not lead to lock. Since the free-running VCO range lies well in the acquisition range, no frequency acquisition aid is necessary in our prototype. Circuit simulations confirm these predictions.

## IV. PHASE NOISE CONSIDERATIONS

The phase noise of the proposed PLL arises from three building blocks, namely the VCO, the XOR gate, and the sampling filter. We wish to design the VCO according to the overall phase noise specification and reduce to negligible levels the XOR and filter contributions.

### A. VCO Phase Noise

The VCO is designed as a three-stage inverter-based ring oscillator. Depicted in Fig. 10, the circuit employs MOS varactors for fine control and banks of switchable capacitors for coarse control. To achieve low flicker-noise-induced phase noise, we choose  $W/L = 36 \mu\text{m}/0.28 \mu\text{m}$  for both PMOS and NMOS devices in each inverter. The varactors have a  $W/L$  of  $26 \mu\text{m}/0.2 \mu\text{m}$ ,<sup>4</sup> providing a tuning range of about 200 MHz, and the capacitor banks consist of twelve 25 fF units, offering a range from 2 to 3 GHz. The circuit draws 3.1 mW from a 1 V supply at 2.4 GHz and exhibits a phase noise of  $-96 \text{ dBc/Hz}$  at 1 MHz offset.

Three aspects of the VCO design merit remarks.

- 1) Simulations suggest that, among various ring oscillator tuning techniques, varactors cause the least degradation in phase noise as the frequency is varied for a given power consumption.<sup>5</sup> In a starved-inverter topology, e.g., the starving transistors themselves contribute significant phase noise as the frequency is decreased.
- 2) As with other inverter-based rings reported in prior work, the VCO suffers from supply sensitivity. In practice, such VCOs are fed from a low-dropout (LDO) regulator. In our prototype, we have used two separate supply pins for the analog and digital sections.
- 3) The three node waveforms within the ring can be combined to generate quadrature phases.<sup>6</sup> A full-size inverter sensing one node and a half-size inverter sensing another can merge their output nodes, generating  $\pm 90^\circ$  or  $180^\circ$  from  $120^\circ$  phases.

The shaping of the VCO phase noise deserves a note as well. Unlike type-II PLLs, a type-I PLL cannot force flicker-noise-induced phase noise to zero at zero frequency. To see this point, we choose a small  $\omega$  in (16) in Appendix I and multiply the magnitude squared of the result by the VCO phase noise profile, e.g.,  $\eta/\omega^3$ , where  $\eta$  is a constant. The PLL output phase noise emerges as  $N^2\omega^2(\eta/\omega^3) = N^2\eta/\omega$ , rising as  $\omega$  falls. Nevertheless, by virtue of its large bandwidth, the proposed PLL still displays a smaller integrated phase noise than a type-II architecture would. Fig. 11 plots the simulated free-running phase noise of the above VCO and the shaping that

<sup>4</sup>Varactor leakage has negligible effect on phase noise, and the variation of  $K_{\text{VCO}}$  affects the phase noise suppression by 1.5 dB.

<sup>5</sup>The varactors occupy 11% of the VCO area.

<sup>6</sup>For more precise quadrature generation, the single-ended ring oscillator in [13] can be used.

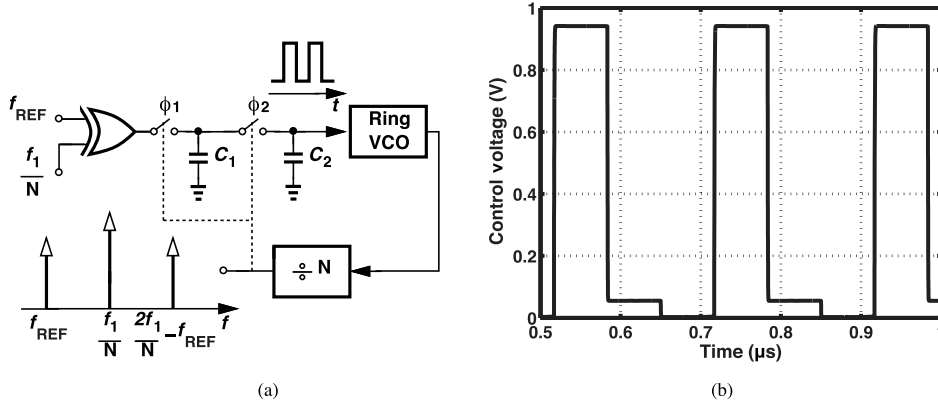


Fig. 9. (a) Proposed PLL in open-loop configuration. (b) Simulated control voltage waveform.

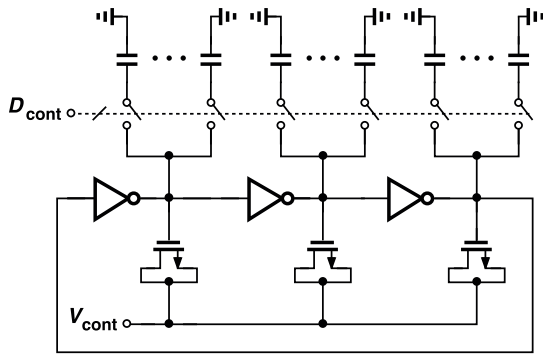


Fig. 10. VCO implementation.

it experiences in the two loops. (Here, the charge-pump PLL is assumed to have a loop bandwidth of  $f_{\text{REF}}/20$ ,<sup>7</sup> while the type-I PLL is based on our architecture with a bandwidth of  $f_{\text{REF}}/2$ .) Our design leads to an integrated phase noise of  $0.35^\circ$  from 100 kHz to 15 MHz, and the type-II loop to  $1.14^\circ$  for the same range.<sup>8</sup> In practice, the charge pump flicker noise makes this comparison more favorable toward the proposed PLL.

### B. PD and MSSF Phase Noise

In order to minimize the contribution of the PD/MSSF cascade in Fig. 4(a), we take several measures. First, the XOR incorporates PMOS and NMOS devices with  $W/L = 32 \mu\text{m}/80 \text{ nm}$  and  $16 \mu\text{m}/80 \text{ nm}$ , respectively, achieving a phase noise of  $-171 \text{ dBc/Hz}$  at 5 MHz offset while consuming  $86 \mu\text{W}$  at 20 MHz. This leads to an in-band phase noise at the PLL output equal to  $-171 \text{ dBc/Hz} + 20 \log N = -129 \text{ dBc/Hz}$ . Second, since  $S_1$  carries large transient currents and can potentially generate high flicker noise, we choose  $W/L = 20 \mu\text{m}/100 \text{ nm}$  for this device. Third, the  $kT/C$  noise associated with  $S_2$  and  $C_2$  is reduced by selecting  $C_2 = 1 \text{ pF}$  ( $C_1 = 16 \text{ pF}$  contributes negligibly). This  $kT/C$  noise translates to in-band phase noise at the PLL output according to  $S_{\text{out,MSSF}} \approx [kT/(2C_2)] f_{\text{REF}}^{-1} N^2 / K_{\text{PD}}^2$ , where the factor of 2 accounts for the fact that  $C_2$  appears in parallel with  $C_1$  ( $\gg C_2$ )

<sup>7</sup>For a reference spur level below  $-60 \text{ dBc}$ , reported type-II PLLs have a bandwidth of no more than  $f_{\text{REF}}/20$ ; hence, this choice for a fair comparison with our architecture.

<sup>8</sup>The peaking in our phase noise can be reduced by choosing a smaller bandwidth. In general, some optimization is necessary at this stage.

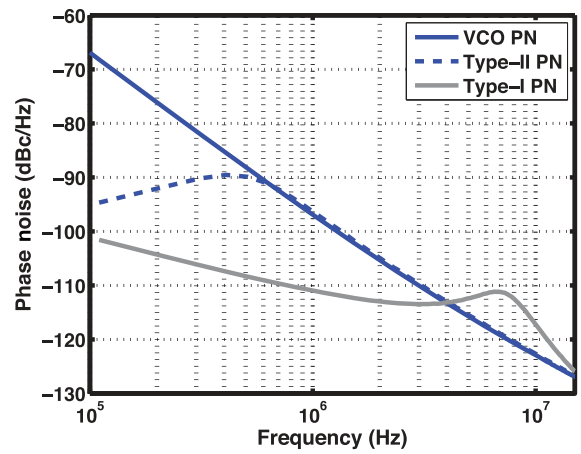


Fig. 11. VCO phase noise in free-running mode and in type-II and proposed PLLs.

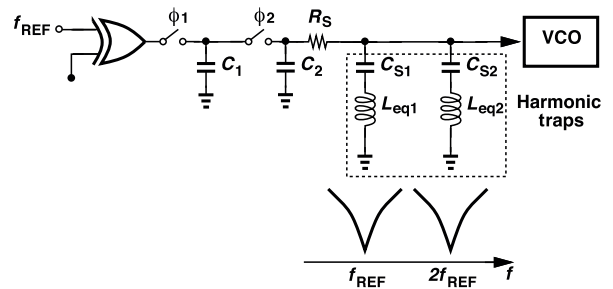


Fig. 12. Concept of harmonic traps.

for about half of the input period. With  $C_2 = 1 \text{ pF}$  and  $K_{\text{PD}} = 2.2 \text{ V/rad}$ , we have  $S_{\text{out,MSSF}} = -126 \text{ dBc/Hz}$ .

The foregoing study also prescribes a design procedure: we first pick the value of  $C_2$  for negligible phase noise contribution and then choose  $C_1$  to be 10–20 times larger. Finally, we size  $S_1$  and the XOR devices for negligible noise as well.

## V. SPUR REDUCTION

Despite the transfer notches introduced by the sampling filter, we observe sidebands on the order of  $-50$  to  $-55 \text{ dBc}$  at the VCO output. This phenomenon arises from three mechanisms. 1) The large VCO varactors ( $W/L = 26 \mu\text{m}/0.2 \mu\text{m}$ ) draw a

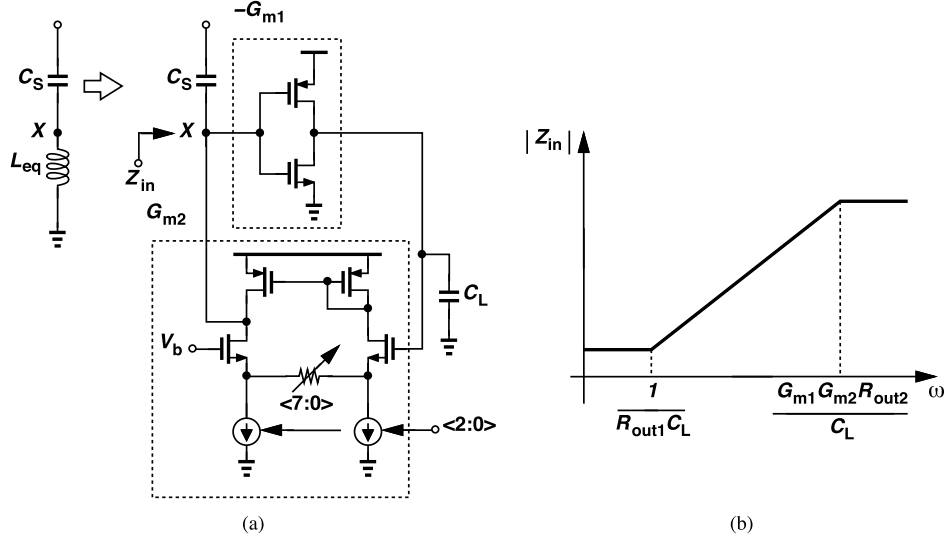


Fig. 13. (a) Harmonic trap implementation. (b) Magnitude of gyration input impedance.

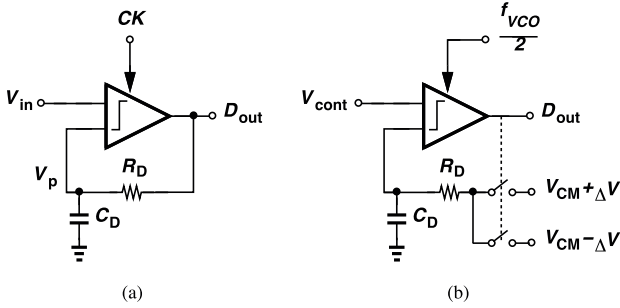


Fig. 14. (a) Traditional and (b) proposed  $\Delta$  modulator architectures.

significant gate leakage current ( $\sim 80$  nA) from  $C_2$  in Fig. 4(a), causing a 2 mV droop in each cycle. 2) The leakage, charge injection, and clock feedthrough of  $S_2$  produce another 1 mV<sub>pp</sub> of ripple. 3) In the presence of ground bond wires, the bounce on the bottom plate of  $C_1$  persists after  $S_2$  turns ON, disturbing the control line periodically.

We propose the use of “harmonic” traps to suppress the ripple with little compromise in the bandwidth. Applicable to any PLL architecture and illustrated in Fig. 12, the idea is to add one or more series resonant branches in parallel with the control line, forming a low impedance to ground at  $f_{REF}$ ,  $2f_{REF}$ , etc.

Harmonic traps entail three issues. 1) Active implementations ultimately present a tradeoff between the trap impedance and the power consumption, potentially unable to fight the MSSF output impedance. For this reason,  $R_S$  ( $\approx 2.5$  k $\Omega$ ) is inserted in Fig. 12. 2) The traps must have a sufficiently high Q so as to contribute negligible phase shift and noise for  $f \leq f_{REF}/2$ . 3) The traps’ resonance frequencies must be calibrated with adequate resolution to deal with PVT variations.

#### A. Harmonic Trap Design

Each trap consists of a capacitor in series with an active inductor, obtained by gyrating another capacitor. As shown in Fig. 13(a),  $G_{m1}$  and  $G_{m2}$  constitute a gyrator, transforming  $C_L$

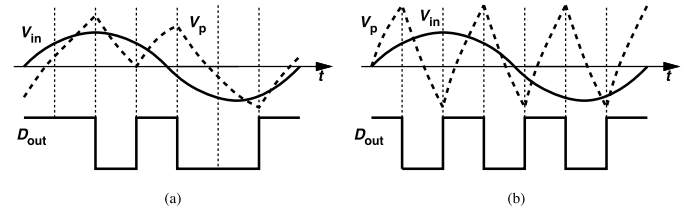


Fig. 15. Effect of  $R_D C_D$  on  $\Delta$  modulator operation. (a) Long time constant. (b) Short time constant.

to  $Z_{in} = L_{eq}s = C_L s / (G_{m1}G_{m2})$  if their output impedances are assumed infinite. For example, the  $f_{REF}$  trap uses  $G_{m1} = 0.92$  mS,  $G_{m2} = 54$   $\mu$ S and  $C_L = 3.5$  pF, creating  $L_{eq} = 70$   $\mu$ H. The degeneration resistance and the bias currents within  $G_{m2}$  are programmable. The power dissipation is 170  $\mu$ W.

For design purposes, we need a more accurate expression for  $Z_{in}$ . If the output impedances of  $G_{m1}$  and  $G_{m2}$  are denoted by  $R_{out1}$  and  $R_{out2}$ , respectively, then  $Z_{in} = (R_{out1}C_L s + 1)R_{out2} / (R_{out1}C_L s + G_{m1}R_{out1}G_{m2}R_{out2} + 1)$ . Plotted in Fig. 13(b),  $|Z_{in}|$  reveals an inductive behavior for  $(R_{out1}C_L)^{-1} < \omega < G_{m1}G_{m2}R_{out2}/C_L$ . It is important that the trap resonance frequency,  $\omega_{res}$ , lie well between the zero and pole frequencies so that  $Z_{in}$  approaches a pure inductor. We therefore view  $(R_{out1}C_L)^{-1} \ll \omega_{res} \ll G_{m1}G_{m2}R_{out2}/C_L$  as a guideline for choosing  $C_L$ . If  $Z_{in}$  is rewritten as  $[C_L s / (G_{m1}G_{m2}) + (G_{m1}G_{m2}R_{out1})^{-1}] \parallel R_{out2}$ , then we recognize that the inductance sees a series resistance equal to  $(G_{m1}G_{m2}R_{out1})^{-1}$  and a parallel resistance equal to  $R_{out2}$ . Since  $R_{out2}$  is sufficiently large in our design, the quality factor is approximately equal to  $R_{out1}C_L\omega$ , about 15 at  $f_{REF} = 20$  MHz. With the large transistor dimensions chosen in this design, the gyrator input-referred offsets are less than 6 mV. To cover PVT variations, the trap frequency has a programmable range of  $\pm 30\%$  around its nominal value with a resolution of 0.6 MHz. Circuit simulations indicate that the traps negligibly affect the loop settling time.

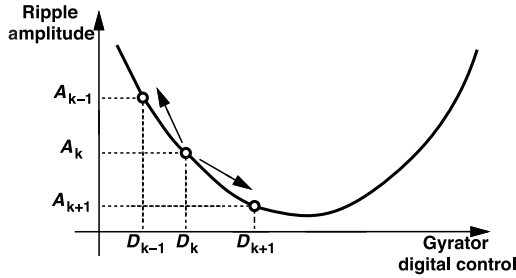


Fig. 16. Notch calibration algorithm.

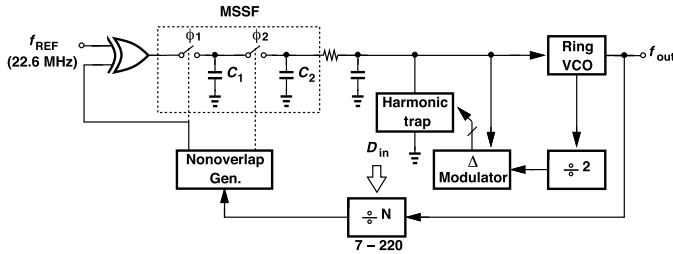


Fig. 17. Final proposed architecture of the synthesizer.

The noise contribution is formulated by modeling the gyrator noise by a current source and subjecting it to a (high-pass) transfer function to  $V_{\text{cont}}$  and another from  $V_{\text{cont}}$  to  $\phi_{\text{out}}$ . Calculations and simulations predict a phase noise of  $-131$  dBc/Hz at 5 MHz offset resulting from the traps.

### B. Notch Calibration

To calibrate the traps, we must seek an error whose value reaches a minimum as the notch frequency reaches the desired value, e.g.,  $f_{\text{REF}}$ . The control ripple amplitude is one such error. But we must also measure this error with reasonable fidelity as, toward the end of calibration, it becomes very small. In our design, e.g., a spur level of  $-60$  dBc at the output is equivalent to a ripple amplitude of about  $0.28$  mV<sub>pp</sub>.

We employ a  $\Delta$  modulator as a compact, low-power ADC to measure the ripple waveform and reconstruct it in the digital domain. Shown in Fig. 14(a), a traditional  $\Delta$  modulator consists of a comparator and a low-pass feedback network, forcing  $V_p$  to track  $V_{\text{in}}$ . As a result, the running average of the pulsewidth-modulated output also tracks  $V_{\text{in}}$ , provided that  $R_D C_D$  is sufficiently long [Fig. 15(a)]. Otherwise, the input peaks do not exceed the peaks of  $V_p$ , causing failure [Fig. 15(b)].

Similarly, the  $\Delta$  modulator of Fig. 14(a) fails for small or slow input swings; it simply generates a periodic output at half of the clock frequency if the input peaks do not exceed the peaks of  $V_p$ . It can be proved that the sensitivity is given by  $V_{\text{DD}}\{1 - \exp[-T_{\text{CK}}/(2R_D C_D)]\}$ , where the comparator output is assumed to swing between 0 and  $V_{\text{DD}}$ . For example, a sensitivity of  $0.28$  mV<sub>pp</sub> with  $f_{\text{CK}} \approx 1.2$  GHz translates to  $R_D C_D = 3$   $\mu\text{s}$ , demanding very large values for  $R_D$  and  $C_D$ . To resolve this issue, we modify the architecture as depicted in Fig. 14(b), where the comparator is clocked at  $f_{\text{VCO}}/2$  and its output drives a 1 bit DAC with a much smaller swing,  $\pm\Delta V$ . A  $\Delta V$  of 25 mV, e.g., allows a 20 fold reduction in the  $R_D C_D$  product. In this design, we have  $R_D = 50$  k $\Omega$ ,  $C_D = 4$  pF, and a StrongArm comparator consuming 80  $\mu\text{W}$ .

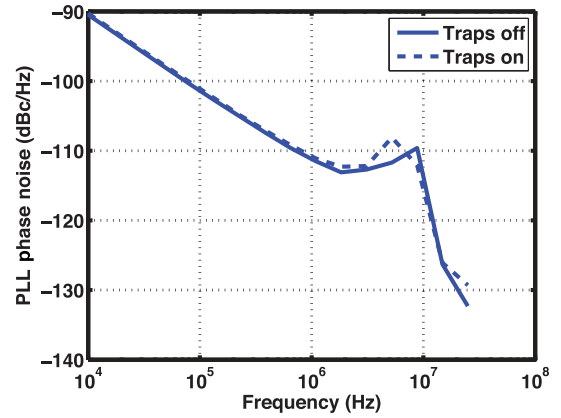


Fig. 18. Simulated PLL phase noise before and after harmonic traps are ON.

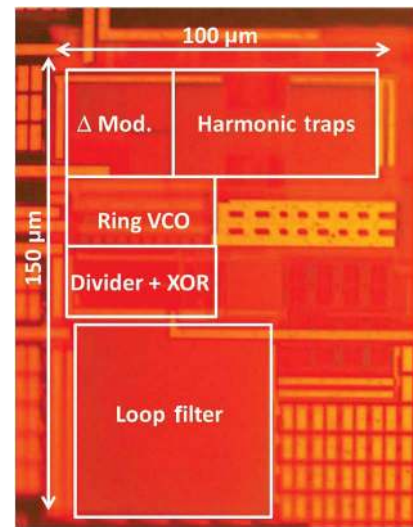


Fig. 19. Die micrograph.

Since the ripple amplitude is a convex function of the trap resonance frequency, we must somehow decide when the calibration has reached a minimum. As shown in Fig. 16, we measure the ripple for three consecutive gyrator codes  $D_{k-1}$ ,  $D_k$  and  $D_{k+1}$  and consider three cases. 1) If  $A_{k-1} > A_k > A_{k+1}$ , we are on the descending slope and must increase the code. 2) If  $A_{k-1} < A_k < A_{k+1}$ , we are on the ascending slope and must decrease the code. 3) If  $A_k < A_{k-1}$  and  $A_k < A_{k+1}$ , then  $D_k$  is the optimum value. The calibration runs in the background and compensates for temperature and supply drifts.

The overall synthesizer architecture is shown in Fig. 17. The feedback divider provides  $N = 7 - 220$ , but only the range from 120 to 124 is used for the 2.4 GHz band. Fig. 18 shows the simulated phase noise plot before and after harmonic traps are ON. As can be seen, the traps contribute negligible phase noise but increases the peaking by 1 dB due to their additional phase shift.

## VI. EXPERIMENTAL RESULTS

The integer-N synthesizer has been fabricated in the TSMC 45 nm digital CMOS technology. As shown in Fig. 19, the die measures  $100 \mu\text{m} \times 150 \mu\text{m}$ . Tested with a 1 V supply, the



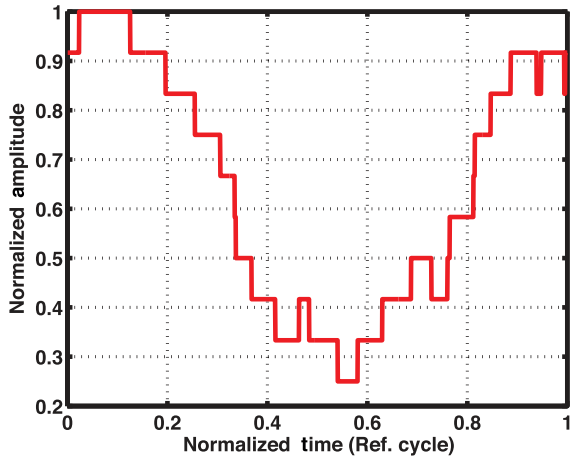


Fig. 20. Reconstructed ripple waveform sensed by  $\Delta$  modulator.

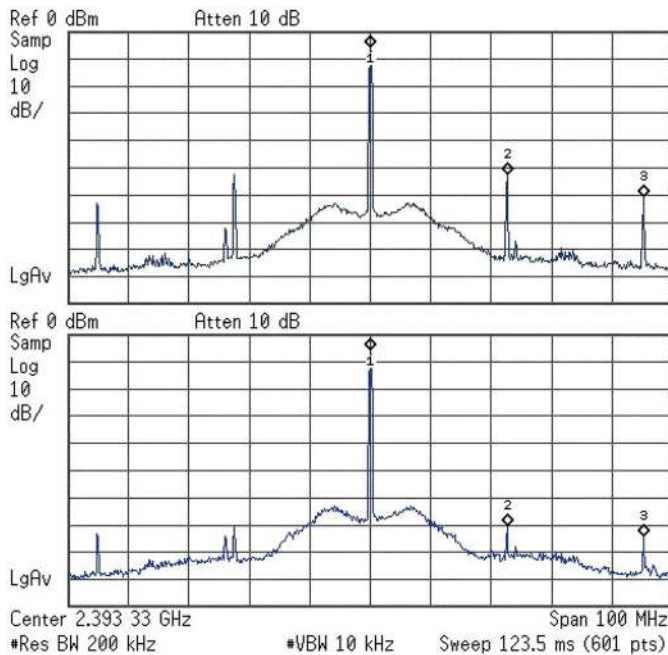


Fig. 21. Measured output spectrum with harmonic traps turned OFF (top) and turned ON (bottom).

synthesizer operates from 2 to 3 GHz and consumes 4 mW at 2.4 GHz. The 22.6 MHz input reference is produced by a low-noise crystal oscillator<sup>9</sup> (hence the departure from 20 MHz) and the output is measured by an Agilent spectrum analyzer. The  $\Delta$  modulator output is sent off-chip and processed in Matlab, and the control codes are written back to the chip through a serial bus.

Upon power-up, the PLL locks with the harmonic traps OFF and then the traps are turned ON and calibrated. The initial calibration takes approximately 400 input cycles, but for subsequent frequency changes (initiated by a modulus change), the calibration settings remain constant because the notch frequencies do not depend on the output frequency. Fig. 20 shows the reconstructed control voltage ripple waveform as sensed by the  $\Delta$  modulator. The output spectra of the

<sup>9</sup> The phase noise is around  $-170$  dBc/Hz at 1 MHz offset.

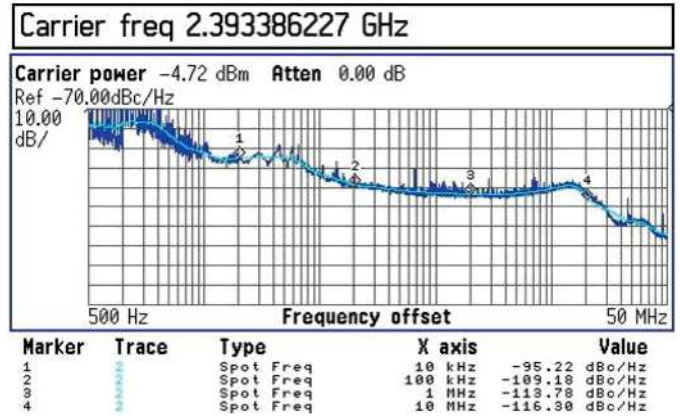


Fig. 22. Measured phase noise.

TABLE I  
PERFORMANCE SUMMARY

	ISSCC'12	ISSCC'14	ISSCC'14	This work
	[14]	[15]	[16]	
Oscillator topology	Ring	Ring	LC	Ring
Reference freq. (MHz)	36	26	48	22.6
Output freq. (GHz)	3.1	2.4	2.3	2.4
Phase noise at 1 MHz offset (dBc/Hz)	-98	-94	-117	-113.8
RMS jitter (ps)	2.23	3.29	0.3	0.97
Integ. range (MHz)	(N/A)	(0.01~40)	(0.01~30)	(0.001~200)
Ref. spur (dBc)	N/A	-75	-55	-65
Power (mW)	25.8	6.4	17.3	4
Area (mm <sup>2</sup> )	0.32	0.013	0.75	0.015
Tech. (nm)	65	40	180	45
FoM <sub>1</sub> (dB)	-218.9	-221.6	-238	-234.1
FoM <sub>2</sub> (dB)	153.7	153.6	171.9	175.4

$$\text{FoM}_1 = 10 \log_{10} \left[ \left( \frac{\text{jitter}}{1 \text{ s}} \right)^2 \left( \frac{\text{power}}{1 \text{ mW}} \right) \right] \text{FoM}_2 = 10 \log_{10} \left[ \left( \frac{f_{\text{osc}}}{\Delta f} \right)^2 \left( \frac{1 \text{ mW}}{\text{power}} \right) \right] - \text{Phase Noise (dBc/Hz)}$$

synthesizer with the harmonic traps OFF and ON are plotted in Fig. 21. The first-order spur falls from  $-47$  to  $-65$  dBc, and the second-order spur falls from  $-55$  to  $-68.5$  dBc. The measured phase noise is shown in Fig. 22. The in-band phase noise reaches  $-114$  dBc/Hz. Integrated from 1 kHz to 200 MHz, the integrated jitter is equal to 0.97 ps<sub>rms</sub>, which satisfies the IEEE 802.11 b/g standard. For all coarse VCO settings from 2 to 3 GHz, the loop is observed to lock.

The measurement is also done with different supply voltages (0.95V, 1.05V). After recalibration, the worst-case reference spur is  $-62$  dBc while the worst-case jitter is 1.14 ps<sub>rms</sub>. Among five measured chips, the phase noise plateau varies by about 1 dB. Table I summarizes the performance of our design and compares it to recently reported synthesizers in the range of 2.3 to 3.1 GHz. The proposed synthesizer achieves an FoM of  $-234.1$  dB based on the integrated jitter and an FoM of 175.4 dB based on the phase noise.

## VII. CONCLUSION

This paper presents an inductorless type-I synthesizer architecture for 2.4 GHz RF applications. A spur reduction approach based on harmonic traps is also introduced that measures the ripple on the control voltage by means of a  $\Delta$  modulator and, using a three-point algorithm, forces the ripple to minimum.

## ACKNOWLEDGMENT

The authors would like to thank the TSMC University Shuttle Program for chip fabrication.

## APPENDIX I

In this appendix, we use the approximation  $[K_{PD}K_{VCO}/(Nj\omega)] \exp(-j\pi fT_{REF})$  to determine the closed-loop bandwidth. From (9), we denote  $K_{PD}K_{VCO}$  by  $K$  and write

$$\left| \frac{\phi_{out}(j\omega)}{\phi_{in}(j\omega)} \right| = \frac{K/\omega}{\left| 1 + \frac{K}{jN\omega} \exp(-j\pi fT_{REF}) \right|} \quad (14)$$

$$= \frac{K/\omega}{\sqrt{N^2\omega^2 - 2KN\omega \sin \pi fT + K^2}}.$$

Equating the square of this quantity to  $N^2/2$  yields the 3 dB bandwidth

$$N^2\omega_{BW}^2 - 2KN\omega_{BW} \sin\left(\frac{\omega_{BW}T_{REF}}{2}\right) - K^2 = 0. \quad (15)$$

Since  $\sin \epsilon \approx \epsilon - \epsilon^3/6$  for  $\epsilon \ll 1$  rad,  $[(KNT_{REF}^3)/24] \omega_{BW}^4 + (N^2 - KNT_{REF})\omega_{BW}^2 - K^2 = 0$ . We also denote  $KT/N = K_{PD}K_{VCO}/(Nf_{REF}) = 2\pi f_{UGB}/f_{REF}$  by  $\alpha$ , obtaining (10).

We should mention that the VCO noise transfer function is obtained as

$$\frac{\phi_{out}}{\phi_{VCO}}(j\omega) = \frac{jN\omega}{j[N\omega - K \sin \pi fT_{REF}] + K \cos \pi fT_{REF}}. \quad (16)$$

## REFERENCES

- [1] L. Kong and B. Razavi, "A 2.4 GHz 4 mW inductorless RF synthesizer," in *IEEE Int. Solid-State Circuits Conf. (ISSCC) Dig. Tech. Papers*, Feb. 2015, pp. 450–451.
- [2] A. A. Abidi, "Phase noise and jitter in CMOS ring oscillators," *IEEE J. Solid-State Circuits*, vol. 41, no. 8, pp. 1803–1816, Aug. 2006.
- [3] A. Homayoun and B. Razavi, "Relation between delay line phase noise and ring oscillator phase noise," *IEEE J. Solid-State Circuits*, vol. 49, no. 2, pp. 384–391, Feb. 2014.
- [4] M. Mikhemar *et al.*, "A cancellation technique for reciprocal-mixing caused by phase noise and spurs," *IEEE J. Solid-State Circuits*, vol. 48, no. 12, pp. 3080–3089, Dec. 2013.
- [5] C. S. Vaucher, "An adaptive PLL tuning system architecture combining high spectral purity and fast settling time," *IEEE J. Solid-State Circuits*, vol. 35, no. 4, pp. 490–502, Apr. 2000.
- [6] S. L. J. Gierink *et al.*, "A 3.5-GHz PLL for fast Low-IF/Zero-IF LO switching in an 802.11 transceiver," *IEEE J. Solid-State Circuits*, vol. 40, no. 9, pp. 49–62, Sep. 2005.
- [7] C. F. Liang *et al.*, "A digital calibration technique for charge pumps in phase-locked systems," *IEEE J. Solid-State Circuits*, vol. 43, no. 2, pp. 390–398, Feb. 2008.
- [8] Z. Cao *et al.*, "0.4 ps-RMS-jitter 13 GHz ring-oscillator PLL using phase-noise preamplification," *IEEE J. Solid-State Circuits*, vol. 43, no. 9, pp. 2079–2089, Sep. 2008.
- [9] M. M. Elsayed *et al.*, "A spur-frequency-boosting PLL with a  $-74$  dBc reference-spur suppression in 90 nm digital CMOS," *IEEE J. Solid-State Circuits*, vol. 48, no. 9, pp. 2104–2117, Sep. 2013.
- [10] S. E. Meninger and M. H. Perrott, "A 1-MHz bandwidth 3.6 GHz 0.18- $\mu$ m CMOS fractional-N synthesizer utilizing a hybrid PFD/DAC structure for reduced broadband phase noise," *IEEE J. Solid-State Circuits*, vol. 41, no. 4, pp. 966–980, Apr. 2006.
- [11] K. J. Wang *et al.*, "Spurious tone suppression techniques applied to a wide-bandwidth 2.4 GHz fractional-N PLL," *IEEE J. Solid-State Circuits*, vol. 43, no. 12, pp. 2787–2797, Dec. 2008.
- [12] B. Razavi, *Principles of Data Conversion System Design*. Piscataway, NJ, USA: IEEE Press, 1995.

- [13] M. Grözinger *et al.*, "CMOS ring oscillator with quadrature outputs and 100 MHz to 3.5 GHz tuning range," in *Proc. 29th Eur. Solid-State Circuits Conf. (ESSCIRC)*, Sep. 2003, pp. 679–682.
- [14] A. Sai *et al.*, "A digitally stabilized type-III PLL using ring VCO with 1.01ps<sub>rms</sub> integrated jitter in 65 nm CMOS," in *IEEE Int. Solid-State Circuits Conf. (ISSCC) Dig. Tech. Papers*, Feb. 2012, pp. 248–249.
- [15] Y. C. Huang *et al.*, "A 2.4 GHz ADPLL with digital-regulated supply-noise-insensitive and temperature-self-compensated ring DCO," in *IEEE Int. Solid-State Circuits Conf. (ISSCC) Dig. Tech. Papers*, Feb. 2014, pp. 270–271.
- [16] P. C. Huang *et al.*, "A 2.3 GHz fractional-N dividerless phase-locked-loop with  $-112$  dBc/Hz in-band phase noise," in *IEEE Int. Solid-State Circuits Conf. (ISSCC) Dig. Tech. Papers*, Feb. 2014, pp. 362–363.



**Long Kong** (S'15) received the B.E. degree in microelectronics from Shanghai Jiao Tong University, Shanghai, China, in 2011, and the M.S. degree in electrical engineering from the University of California (UCLA), Los Angeles, CA, USA, in 2013. He is pursuing the Ph.D. degree at UCLA, where he is developing high-performance frequency synthesizer architectures.

Mr. Kong is the recipient of the Qualcomm Innovation Fellowship (2013–2014), the Analog Devices Outstanding Student Designer Award (2015), and the Broadcom Fellowship (2015–2016).



**Behzad Razavi** (F'03) received the B.S.E.E. degree from Sharif University of Technology, Tehran, Iran, in 1985, and the M.S.E.E. and Ph.D.E.E. degrees from Stanford University, Stanford, CA, USA, in 1988 and 1992, respectively.

He was with AT&T Bell Laboratories, Murray Hill, NJ, USA, and Hewlett-Packard Laboratories, Palo Alto, CA, USA, until 1996. Since 1996, he has been an Associate Professor and subsequently Professor of Electrical Engineering with the University of California, Los Angeles, CA, USA. He was an Adjunct Professor with Princeton University, Princeton, NJ, USA, from 1992 to 1994, and Stanford University, Stanford, CA, USA, in 1995. He is the author of *Principles of Data Conversion System Design* (IEEE Press, 1995), *RF Microelectronics* (Prentice Hall, 1998, 2012) (translated to Chinese, Japanese, and Korean), *Design of Analog CMOS Integrated Circuits* (McGraw-Hill, 2001) (translated to Chinese, Japanese, and Korean), *Design of Integrated Circuits for Optical Communications* (McGraw-Hill, 2003, Wiley, 2012), and *Fundamentals of Microelectronics* (Wiley, 2006) (translated to Korean and Portuguese), and the editor of *Monolithic Phase-Locked Loops and Clock Recovery Circuits* (IEEE Press, 1996), and *Phase-Locking in High-Performance Systems* (IEEE Press, 2003). His research interests include wireless transceivers, frequency synthesizers, phase-locking and clock recovery for high-speed data communications, and data converters.

Prof. Razavi served on the Technical Program Committees of the International Solid-State Circuits Conference (ISSCC) from 1993 to 2002 and VLSI Circuits Symposium from 1998 to 2002. He has also served as a Guest Editor and Associate Editor of the IEEE JOURNAL OF SOLID-STATE CIRCUITS, the IEEE TRANSACTIONS ON CIRCUITS AND SYSTEMS, and *International Journal of High Speed Electronics*. He has served as the IEEE Distinguished Lecturer. He was the recipient of the Beatrice Winner Award for Editorial Excellence at the 1994 ISSCC, the Best Paper Award at the 1994 European Solid-State Circuits Conference, the Best Panel Award at the 1995 and 1997 ISSCC, the TRW Innovative Teaching Award in 1997, the Best Paper Award at the IEEE Custom Integrated Circuits Conference in 1998, and the McGraw-Hill First Edition of the Year Award in 2001. He was the corecipient of both the Jack Kilby Outstanding Student Paper Award and the Beatrice Winner Award for Editorial Excellence at the 2001 ISSCC. He was the recipient of the Lockheed Martin Excellence in Teaching Award in 2006, the UCLA Faculty Senate Teaching Award in 2007, and the CICC Best Invited Paper Award in 2009 and in 2012. He was the corecipient of the 2012 VLSI Circuits Symposium Best Student Paper Award and the 2013 CICC Best Paper Award. He was also recognized as one of the top 10 authors in the 50-year history of ISSCC. He was the recipient of the 2012 Donald Pederson Award in Solid-State Circuits and the American Society for Engineering Education PSW Teaching Award in 2014.